Experimental and Numerical Investigation of Secondary Flow Structures in an Annular LPT Cascade under Periodical Wake Impact

Benjamin Winhart, Martin Sinkwitz, Andreas Schramm, David Engelmann, Francesca Di Mare, Ronald Mailach

Experimental and Numerical Investigation of Secondary Flow Structures in an Annular LPT Cascade under Periodical Wake Impact – Part 2: Numerical Results

Benjamin Winhart[1]*, Martin Sinkwitz[1], Andreas Schramm[1], David Engelmann[1], Francesca di Mare[1], Ronald Mailach[2]

ISROMAC 2017

International Symposium on Transport Phenomena and Dynamics of Rotating Machinery

Maui, Hawaii

December 16-21, 2017

Abstract

In this work we present the results of the numerical investigations of periodic wake-sekondary flow interaction carried out on a low pressure turbine (LPT) equipped with modified T106-profile blades. The numerical predictions obtained by means of unsteady Reynolds-Averaged Navier-Stokes (URANS) simulations using a k-ω-model have been compared with measurements conducted in the same configuration and discussed in part 1 of this 2-part work. The Q-criterion has been employed to characterize the secondary flow structures and accurately identify their origin. Based on these information a correlation between the time-dependent interactions of the incoming wakes and the vortex structures is proposed and discussed.

Keywords

secondary flow structures — low pressure turbine — wake interaction

[1] *Chair of Thermal Turbomachines, Ruhr-Universität Bochum, Bochum, Germany*

[2] *Chair of Turbomachinery and Flight Propulsion, Technische Universität Dresden, Dresden, Germany*

*__Corresponding author__: Benjamin.Winhart@rub.de

INTRODUCTION

The numerical prediction of interaction effects between incoming wakes and secondary flow structures is challenging as the participating flow phenomena are highly unsteady and three dimensional. This paper discusses the capability of URANS simulations in predicting interaction mechanisms between periodically incoming wakes and the secondary flow system inside a modified, low speed, annular T106 turbine stator test facility located at the Chair of Thermal Turbomachines at Ruhr-Universität Bochum.

Over the years a wide range of experimental and numerical studies about the T106 secondary flow system interacting with periodically incoming wakes has been carried out. Schulte and Hodson [1] investigated the impact on loss generation and found that the wake-boundary layer interaction can reduce profile losses by suppressing suction side boundary layer separation. Michelassi *et al.* investigated the impact of incoming wakes on losses of a linear T106A cascade using direct numerical simulations (DNS) and large eddy simulations (LES) [2, 3, 4, 5]. They found that the incoming wake dilation can account for 25% of the overall 2-dimensional passage losses. They also highlighted the effect of varying reduced frequency F_{red} and flow coefficient ϕ on the wake flow path and thus on the overall losses. In an experimental and numerical investigation of the flow through a linear T106 low-pressure turbine cascade Koschichow *et al.* focused on the complex flow phenomena near the end wall region of the cascade with and without the influence of incoming wakes [6, 7]. They found that the incoming wakes periodically reduce secondary flow and suppress the propagation of the horseshoe vortex and the passing wakes induce additional vortex structures which interact with the crossflow. The majority of the aforementioned works focus on linear cascades. However, some important flow features present in real turbomachines flow can not be considered in such configurations.

In a two part research work we present the investigations of an annular low-speed LPT which provides excellent access possibilities and where spatially and temporally highly resolved measurements could be obtained. In part 2 of this study the capability of 3-dimensional URANS simulations to predict the complex interaction mechanisms involved in the flow inside the investigated stator row is assessed. The turbine is equipped with a modified T106^{RUB} stator blading to match the characteristics of the well known and frequently investigated T106 profile under low Mach-number flow. Based on the numerical results an analysis of the 3-dimensional flow field is conducted in order to gain insight in the secondary

flow structures. The interaction mechanisms between the periodically incoming wakes and the secondary flow structures are further analyzed through an investigation of the kinematics of the incoming wakes based on of flow coefficient ϕ and Strouhal number Sr in one configuration. Finally a link between wake impacted secondary flow structures and total pressure loss distributions is proposed.

1. NUMERICAL SETUP

In this chapter the test case as well as the numerical model, boundary conditions and the numerical setup are briefly described. Finally the solution method is summarized.

1.1 Test Case Description

The test case chosen for this study is a large scale low speed axial turbine test rig, located at the chair of Thermal Turbomachines of Ruhr-Universität Bochum. The annular test rig consists of an inlet guide vane (IGV) row, a rotating wake generator row and the investigated stator row equipped with a newly designed T106^{RUB} LPT blading to match the characteristics of the T106 profile at low speed conditions. An isometric view of the above mentioned relevant parts is shown in figure 1 with the rotating parts highlighted in red. The main test rig parameters are summarized in table 1. A more detailed description of the test case is given in [8] and in [9].

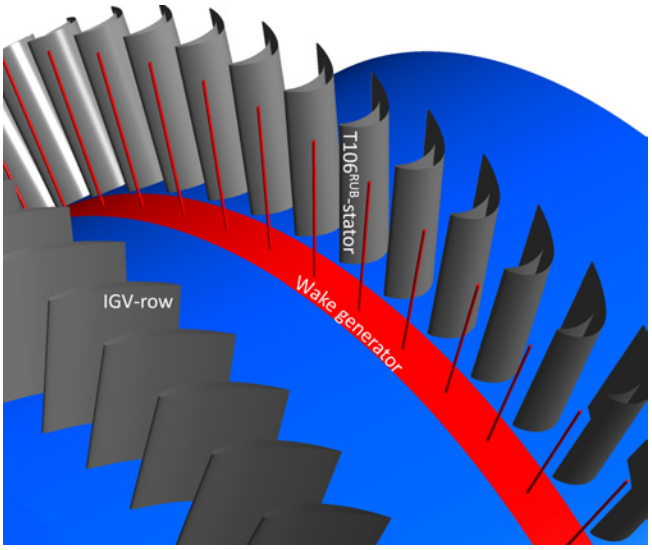

Figure 1. Isometric view of the test rig's relevant parts including IGV, rotating wake generator (red) and investigated T106^{RUB} stator row

1.2 Numerical Model & Boundary Conditions

The numerical domain is shown in Figure 2 for the configuration with 60 wake generator bars. In order to save computational cost and reduce modeling inaccuracies the IGV row is not included in the numerical domain. However, as it is very important to take the effects of the wakes generated by the IGV into account, highly resolved 2-dimensional boundary conditions (BCs) were measured downstream the IGV and imposed at the domain inlet (Fig. 2). These encompass total pressure, velocity direction and turbulence intensity. At the outlet the mass flow rate is adjusted to match the measured axial flow velocity. As the number of wake generators as well as the blade count of the stator is 60, simple periodic BCs can be set in circumferential direction.

Table 1. Main test rig parameters

Test rig		
Outer diameter (Casing)	D_C	1.66 m
Inner diameter (Hub)	D_H	1.32 m
Mass flow	$\dot{m}$	12.8 kg/s
Operating point, Design point		
Reynolds number (exit. theor.)	$Re_{exit,th}$	200,000
Mach number (exit. theor.)	$Ma_{exit,th}$	0.091
Strouhal number range	Sr	0.60 - 3.15
Flow coefficient range	ϕ	0.81 - 2.84

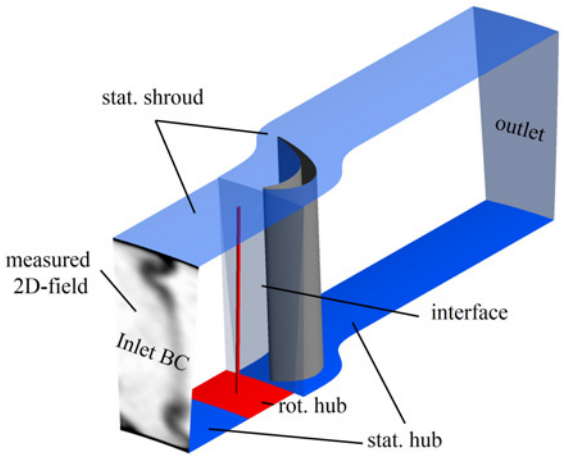

Figure 2. Numerical domain with visualized total pressure inlet BC

1.3 Numerical Mesh & Time Step

The vortex-structures resulting from the influence of incoming wakes on secondary flow are inherently three dimensional and unsteady. This leads to increased demands on the numerical mesh in all spatial directions. The mesh for the wake generator domains has been created using ANSYS ICEM, while the T106^{RUB} has been meshed with ANSYS TurboGrid. The objective was to create as cubical cell volumes as possible in the area of the vortex generators and the T106^{RUB} stator row. The final mesh consists of approximately 7.21 million cells. The main mesh parameters are summarized in table 2, where d_w represents the first cell offset at all wall surfaces, n_p and n_r stand for the number of cells along the blade profile and along the radial direction and n for the total cell count.

Time step and mesh size sensitivity studies revealed that 128 time steps per wake generator bar passing are sufficient to resolve all relevant frequencies. This leads to a minimum time step of $\Delta t = 2.1701 \cdot 10^{-5}$ s and a maximum time step of $\Delta t = 1.3021 \cdot 10^{-4}$ s depending on Sr and ϕ.

Table 2. Summary of important mesh parameters

	d_w [m]	n_p	n_r	n
WG	$5 \cdot 10^{-6}$	60	170	2.10 m.
T106	$5 \cdot 10^{-6}$	415	160	5.11 m.
total				**7.21 m.**

1.4 Solution Method

The calculations presented in this paper have been performed using ANSYS CFX release 18.2. In ANSYS CFX the RANS equations are solved using a pressure-based, coupled, unstructured finite-volume algorithm [10]. The solver is implicit in time using a second order backward Euler discretization. For convergence acceleration a coupled algebraic multi-grid method is used to solve the discrete system of flow equations [11]. All steady and unsteady simulations were performed using the shear stress transport (SST) Menter two equation turbulence model [12]. To capture transitional effects, the γ-transition model is used [13], which is a further development of the widely used γ-Re_θ-transition model.

2. RESULTS AND DISCUSSION

In this section the numerical predictions are compared with experimental data and discussed.

2.1 Static Pressure Distribution

The development of secondary flow structures is strongly affected by the blade loading. To verify that the same blade loading as in the experimental test rig is also reproduced in the calculations, the distribution of pressure coefficient

$$c_p = \frac{p(x) - p_1}{p_{t,1} - p_1} \tag{1}$$

at 50% span is compared to experimental data. The results are shown in Figure 3 and are in a good overall agreement with slight deviations in the aft pressure side distribution.

2.2 Integral Flow Values

Integral flow values are compared in this section to verify the correspondence of the operating conditions in the numerical calculations. The inflow axial velocity $c_{x,1}$, outflow absolute velocity c_2 and outflow absolute velocity flow angle α_2 are shown in Table 3 for one operating point and show also a very good agreement between simulations and experiments. Both velocities are related to the stationary frame as well as α_2.

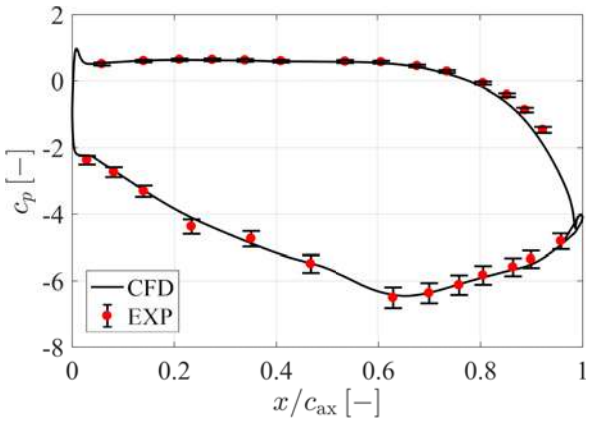

Figure 3. Comparison of experimentally and numerically achieved pressure coefficient c_p at 50% span ($Sr = 1.35$, $\phi = 0.97$); experimental data are shown with error bars of 95% confidence interval

Table 3. Comparison of integral flow values

	$c_{x,1}$ [m/s]	c_2 [m/s]	α_2 [°]
EXP	13.6	30.6	153.6
CFD	13.7	30.6	153.6
Δ [%]	0.3	0.0	0.0

2.3 2-Dimensional Field Traverse Data

In this section the computational time averaged field data of velocity ratio $\overline{c}/\overline{c}_{ax}$, total pressure loss coefficient $\overline{\zeta}_p$ and vorticity $\overline{\omega}_x$ are compared with results obtained by means of 5 hole probe (5HP) traverse measurements at $0.34 \cdot C$ downstream of the T106^{RUB} stator trailing edge (plane 3.2 shown in figure 4), where C represents the chord length of the investigated stator blade. The distributions are shown in figure 5 in comparison with the experimental data. The viewing direction is in upstream direction.

Velocity c**:** The distribution of time averaged absolute velocity $\overline{c}$ is predicted very well by the CFD. The free stream velocity field reveals the same topologies of high velocity fluid ($0 \leq r/H \leq 0.2$), medium velocity fluid ($0.2 \leq r/H \leq 0.8$) and low velocity fluid ($0.8 \leq r/H \leq 1$) compared to the

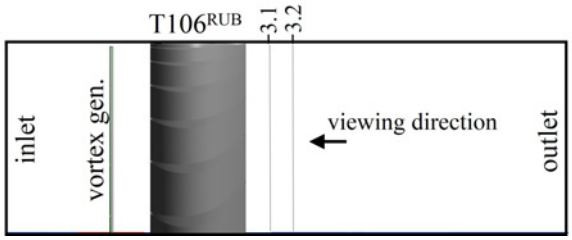

Figure 4. Schematic meridional view of numerical domain and measurement planes downstream T106^{RUB} stator trailing edge

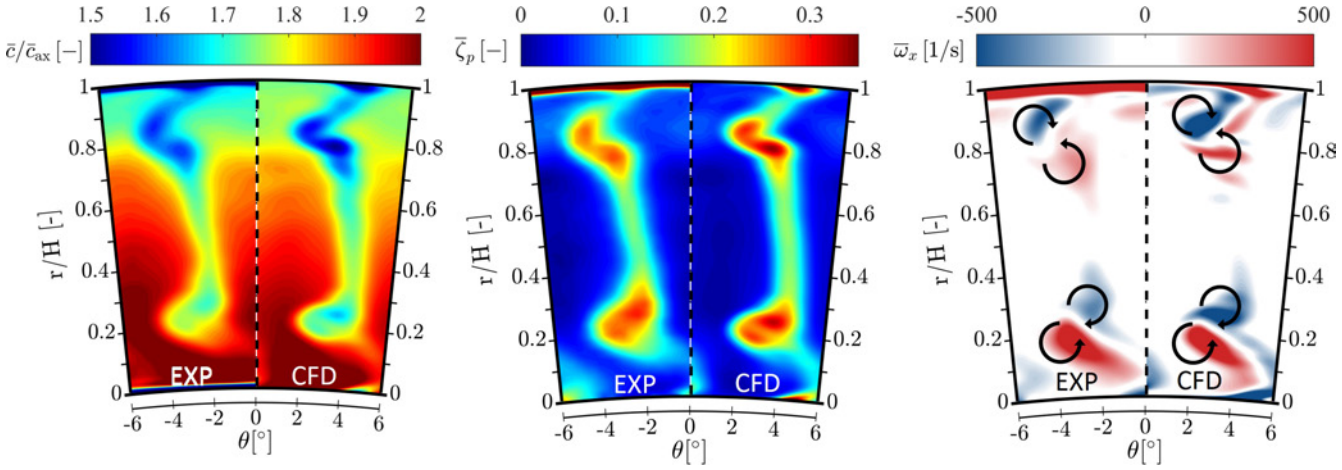

Figure 5. Distribution of velocity field data $\overline{c}$, total pressure loss coefficient $\overline{\zeta}_p$ and vorticity $\overline{\omega}_x$ at $Sr = 1.35$, $\phi = 0.97$ in measurement plane 3.2 at $0.34 \cdot C$ downstream of T106$^{\text{RUB}}$ stator's trailing edge (view in upstream direction)

experimental data. The velocity drop caused by the profile losses in the areas of the stator wakes is also depicted very well by the numerical prediction. In the areas of secondary flow structures the deficit of velocity is captured well by CFD. The extension of the lower loss region is a little more extended in radial direction in the experiment and thus shows a slighlty higher core velocity. The topology of the upper secondary loss region is consistent with the measurement data. Both cores with high velocity drops are captured by the CFD although the numerical data show a slightly higher drop in velocity. The connection between the upper core and shroud is a little less distinct in the numerical data.

Total pressure loss coefficient ζ_p: The distribution of time averaged total pressure loss coefficient

$$\overline{\zeta}_p = \frac{\overline{p}_{t,1} - \overline{p}_t(r,\theta)}{\overline{p}_{t,1} - \overline{p}(r,\theta)} \tag{2}$$

shows a consistent structure between experiment and CFD, similar to the velocity field. The loss levels in the areas of profile losses and secondary flow are described very well while the the lower loss region shows a larger radial extension in the experimental data. The freestream loss is also in good agreement.

Vorticity ω_x: Vorticity is a quantity which describes the local spinning motion of a continuum. It can be invoked to get a basic idea of the secondary vortex systems in turbomachines, although this method can not distinguish between swirling motions and shearing motions. In Cartesian coordinates the axial vorticity is given by:

$$\overline{\omega}_x = \left(\frac{\partial \overline{c}_z}{\partial y} - \frac{\partial \overline{c}_y}{\partial z} \right). \tag{3}$$

The comparison between experimental and numerical data shows that the main vorticity distribution is captured well by CFD, although it reveals slight deviations in the upper counter clockwise rotating area.

3. IDENTIFICATION OF SECONDARY FLOW STRUCTURES

3.1 General Description

To gain a better understanding of the different vortices which constitute the secondary flow system, an analysis of the 3D flow field is conducted. A valuable quantity to visualize vortex structures is provided by the Q-criterion which is defined as the second invariant of the velocity gradient tensor $\partial u_i / \partial x_j$:

$$Q = \frac{1}{2} \left(\Omega_{ij} \Omega_{ij} - S_{ij} S_{ij} \right) \tag{4}$$

with

$$\Omega_{ij} = \frac{1}{2} \left(\frac{\partial u_i}{\partial x_j} - \frac{\partial u_j}{\partial x_i} \right) \quad \text{and} \quad S_{ij} = \frac{1}{2} \left(\frac{\partial u_i}{\partial x_j} + \frac{\partial u_j}{\partial x_i} \right), \tag{5}$$

where Ω_{ij} is the vorticity tensor and S_{ij} is the rate-of-strain-tensor. Thus, in contrast to the aforementioned vorticity, the Q-criterion represents the local balance between shear strain rate and vorticity magnitude, defining vortices as areas where the vorticity magnitude is greater than the magnitude of strain rate [14].

The main vortex structures participating in the secondary flow system of the investigated T106$^{\text{RUB}}$ stator are visualized in figure 6 at two different angles of view via a 3-dimensional iso surface of time averaged Q-criterion. This helps tracing the origins and trajectories of individual vortices. The iso surface is colored with the axial vorticity ω_x to provide an impression of the direction of rotation of each vortex.

Utilizing the information obtained by the 3-dimensional field analysis, an overview of the vortex structures on the evaluation plane 3.1 downstream the T106$^{\text{RUB}}$ stator is presented in figure 7. This provides a better indication of the vortex structure expansion and relative positions inside the annulus. In addition, the findings of this analysis build a basis for the interpretation of the experimentally achieved vorticity distributions presented in [8].

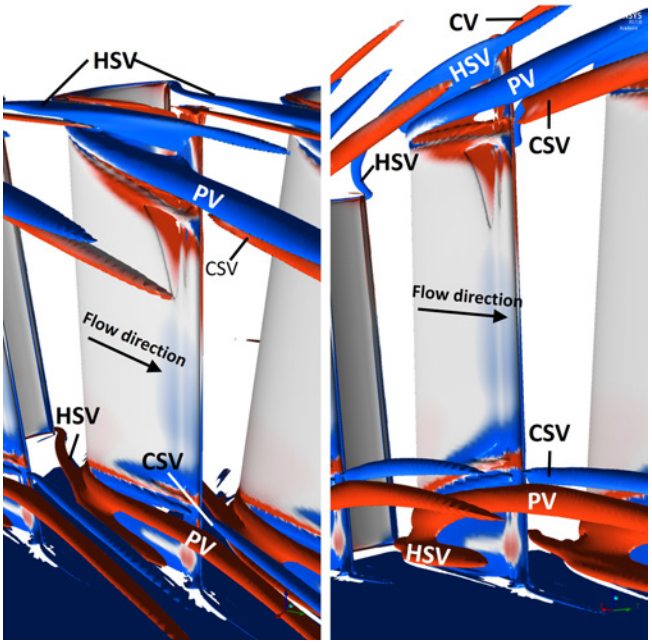

Figure 6. Secondary flow structures for $Sr = 1.35$, $\phi = 0.97$ visualized using time averaged Q-criterion iso surface at $\overline{Q} = 2 \cdot 10^5$ 1/s colored with vorticity ω_x

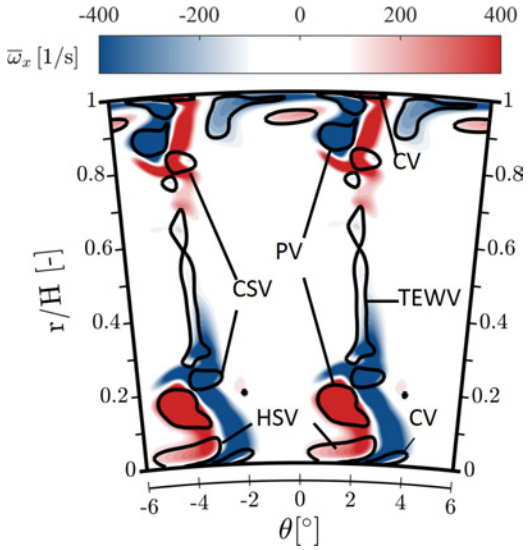

Figure 7. Contour plot of time averaged vorticity $\overline{\omega}_x$ with isolines of time averaged Q-criterion $\overline{Q} = 2 \cdot 10^5$ 1/s at measurement plane 3.1 ($Sr = 1.35$, $\phi = 0.97$)

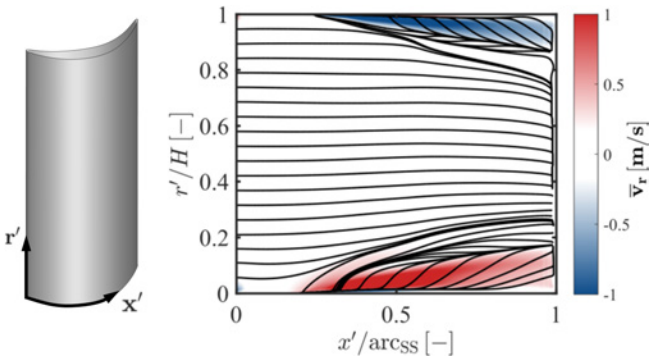

Figure 8. Streamlines of time averaged velocity $\overline{v}$ along the blade suction side transformed into the x'-r'-plane at $Sr = 1.35$, $\phi = 0.97$; contour showing velocity component $\overline{v}_{r'}$

3.2 Interpretation

Passage Vortex (PV): The passage vortex is a main component of the secondary flow system in turbomachines. The PV is the direct consequence of secondary flow caused by the blade flow turning and forms in the hub region as well as in the shroud region. Concerning the 3-dimensional flow field the PV originates inside the passage and propagates towards mid-span direction due to a strong corner separation which induces a radial crossflow (figure 8). The 2-dimensional analysis of the PV dimensions in the investigated test case reveals that the PV on the hub side has a bigger expansion than the PV on the shroud side. This can be addressed to the lower velocity magnitude near the shroud caused by the radial equilibrium resulting in a less developed secondary flow compared to the hub region.

Concentrated shed vortex (CSV): The concentrated shed vortex is an indirect consequence of the secondary flow which peels off the boundary layer fluid as it impinges the blade suction side. This separated flow region results in corner separations (figure 8) which lead to the concentrated shed vortex. Analysis of the 3-dimensional flow field reveals that in contrast to the PV the CSV originates along the blade edge separation line and has an opposite rotational direction.

Horseshoe vortex (HSV): The horseshoe vortex originates at the blade leading edge. Due to the low impulse of boundary layer fluid, two counter rotating vortices are generated near the blades stagnation point and are convected through the passage. Due to the prevailing pressure gradient the pressure side leg of the HSV is convected towards the neighboring blade's suction side (cf. figure 6) and interact with the PV, which has the same direction of rotation. The suction side leg propagates along the blade surface and connects with the corner vortex (CV). In the present test case the pressure side HSV interacts with the PV but remains visible in the structure of the resulting vortex system which can be explained by the momentum of the HSV fluid which is strong enough to withstand the momentum of the fluid transported inside the PV. Due to the stronger corner separation near the blade hub and the subsequent radial deflection of the PV, the HSV has more room to spread between PV and hub, which results in a more expanded HSV (cf. figure 7).

Corner vortex: The corner vortex acts as a balancing vortex between the PV, blade and endwalls, thus it has an opposite sense of rotation as the PV. As mentioned above the CV and the suction side leg of the HSV connect and are not distinguishable downstream of the blade. The resulting vortex is very small compared to the other vortices but is still notice-

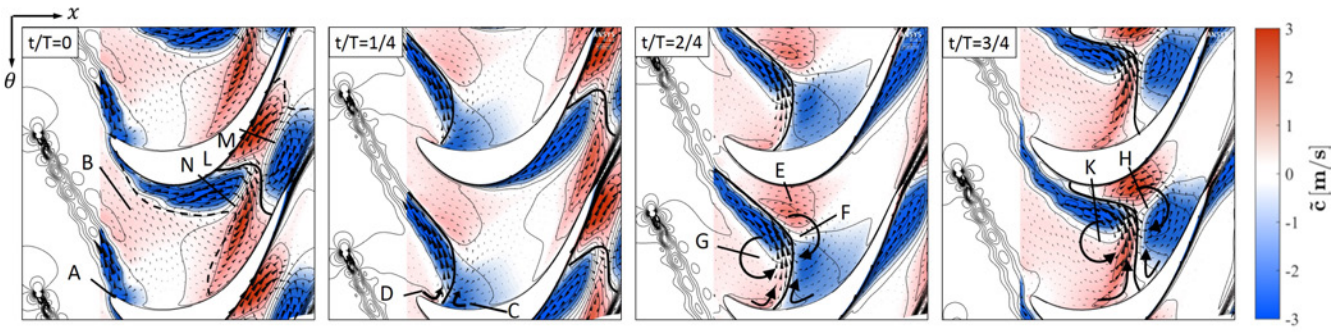

Figure 9. Temporal evolution of wake kinematics at 50% constant span visualized via contours of velocity fluctuation $\tilde{c}$ at $Sr = 1.35$, $\phi = 0.97$; black arrows represent the projected velocity fluctuation vectors

able in the vorticity distribution while it creates a shear layer between the counter rotating vortex structures consisting of PV & HSV and CV/HSV & CSV. The advantage of utilizing the Q-criterion becomes clear at this point as it is not possible to distinguish between the individual vortex structures by solely analyzing the vorticity distribution.

Trailing edge wake vortices (TEWV): The trailing edge wake vortices originate from the shear layer, starting at the blade trailing edge. Fluid from from suction side and pressure side have different momentum and radial velocity components which results in wake vortices being shed along the blade trailing edge.

4. WAKE KINEMATICS

In this chapter the kinematics of the incoming wakes are discussed. Figure 9 shows a temporal evolution of the distribution of velocity fluctuation

$$\widetilde{c} = c(x, \theta, t) - \overline{c}(x, \theta) \tag{6}$$

caused by the incoming wakes at four equally distributed time steps per bar passing on a surface at 50% span. The projected velocity fluctuation vectors are superimposed as black arrows in order to indicate the direction of the induced wake influence.

t/T = 0: At this point of time the incoming wakes impinge on the pressure side of the T106$^{\text{RUB}}$ stator right behind the leading edge (A). Inside the wake an adverse velocity fluctuation is induced due to the prevalent total pressure drop, which causes a negative jet. Due to the blockage caused by the incoming wake an area of accelerated flow appears above the upper boundary of the wake (B).

t/T = 1/4: The incoming wake has propagated further into the passage within this snapshot. At the pressure side of the blade the wake front is pushing a region of decreased velocity (C) due to the fluid transport caused by the negative jet effect (highlighted by curved arrows), whilst behind the wake the near wall velocity is increased (D). The wake shape is slightly bowed (highlighted by a black curve) because of the low momentum fluid near the blade surface and higher passage flow velocity.

t/T = 2/4: The wake moves closer to the upper blade suction side which causes the fluid in this area to accelerate further (E). In the presence of the upper blade potential field the wake gets deflected and attaches to its suction side, which additionally increases the wake bow. In front of the wake a clearly distinguishable, clockwise rotating vortex structure is observable (F) which balances the crossflow fluctuations induced by the negative jet. This vortex causes a velocity reduction at the blade pressure side while it increases the velocity at the neighboring blade suction side. Behind the wake a counter clockwise rotating vortex (G) has the opposite influence on the near wall flow.

t/T = 3/4: Due to the contraction of the passage and the consequently rising convection velocity the wake gets further dilated. Additionally the vortices upstream (H) and downstream (K) of the wake get intensified resulting in higher induced velocity fluctuations. The front part of the upper blade suction side is covered with low momentum fluid as the wake further bends over its surface.

t/T = 4/4 ∨ 0: This point refers to the left-most picture at $t/T = 0$ again, but to the wake further downstream (L) of the one described above. Compared to the previous snapshot the wake bow has further increased as well as the intensity of the counter rotating vortices (M,N). The area influenced by the wake is marked by dashed black lines and stretches almost throughout half the passage due to the increasing wake dilation. The area of negative velocity fluctuation (blue) in front of the wake is about to be convected through the first evaluation plane (3.1), which is located at the right boundary of the figure.

t/T = 5/4 ∨ 1/4: The blue area of negative velocity fluctuation in front of the wake now propagates through the evaluation plane whilst the red area at the neighboring blade suction side is directly in front of it. As the four wake affected cells have already passed the lower blade surface, they are now bounded by the stator's wake.

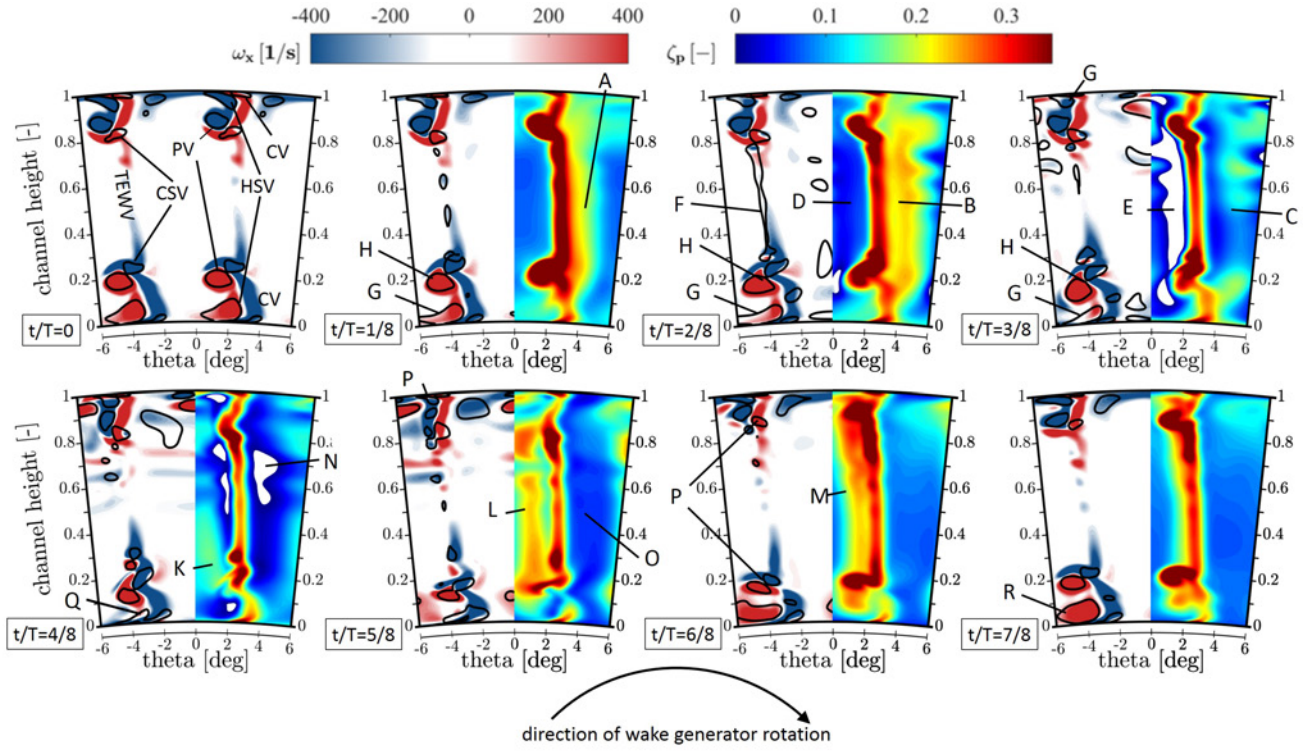

Figure 10. Temporal evolution of secondary flow structures visualized via isolines of Q-criterion $Q = 2 \cdot 10^5$ 1/s and contours of axial vorticity ω_x (left) and contours of total pressure loss coefficient ζ_p at $Sr = 1.35$ and $\phi = 0.97$ at measurement plane 3.1 ($0.15 \cdot C$ downstream T106$^{\text{RUB}}$ TE)

5. TEMPORAL EVOLUTION OF SECONDARY FLOW STRUCTURES & LOSS REGIONS

In this section the temporal evolution of secondary flow structures and loss regions under the influence of periodically incoming wakes is discussed for one combination of Strouhal number Sr and flow coefficient ϕ. Figure 10 shows contours of axial vorticity ω_x and isolines of Q-criterion at $Q = 2 \cdot 10^5$ 1/s on the left side of each plot. On the right side the corresponding distribution of pressure loss coefficient ζ_p is shown. The direction of view is in upstream direction.

The development of the individual vortices is discussed subsequently for eight equally distributed time steps within one bar passing t/T. As the underlying interaction mechanisms are highly complex and coupled, it is not always possible to reduce the explanation of these mechanisms to one fundamental process. Therefore, it is important to understand that the observable fluctuations of the participating vortex systems inside the evaluation plane are not only triggered by the wake as it crosses this evaluation plane, but also by the impact of these wakes on the boundary layers at blade and endwalls, as well as on the vortices inside the passage. These indirect effects occur further upstream and, consequently, it is not always possible to attribute them to the direct effect of the wake inside the evaluation plane.

As boundary layer investigations are not part of this paper the subsequent analysis focuses on the aforementioned direct effects of incoming wakes on the secondary flow system. The wake affected flow propagates through the passage and carries cells of lower and higher momentum fluid (figure 9), which correlates to lower and higher total pressure. As a consequence also the static pressure distribution gets distorted which directly influences the vortex structures due to the prevalent pressure gradient. In addition cells of high total pressure temporarily decrease the local total pressure loss as they pass the evaluation plane, whereas cells of low total pressure increase it.

To help further the interpretation, the bar passing period is divided into three phases. Within the first phase the vortex in front of the incoming wake passes the evaluation plane. In the present case the first phase spreads from $1/8 \leq t/T \leq 3/8$, which is deducible from the distribution of total pressure loss coefficient ζ_p (right side of each plot) as well as from the distribution of velocity fluctuations shown in figure 9, which coincide directly with regions of higher and lower total pressure. Within the second phase ($4/8 \leq t/T \leq 6/8$) the vortex behind the incoming wake is convected through the evaluation plane. Inside the third phase almost no wake affected fluid passes the evaluation plane ($0 \leq t/T \leq 7/8$).

Phase 1 ($1/8 \leq t/T \leq 3/8$): Within this section the two cells of wake influenced fluid in front of the wake start to propagate through the evaluation plane. At first the pressure sided cell of low total pressure propagates through the evaluation plane (cf. figure 9). This is clearly visible in the total pressure loss distribution shown in figure 10 at time step $t/T = 1/8$,

indicated by high values of ζ_p at the pressure side boundary of the stator's wake (A). This cell is intensified until time step $t/T = 2/8$ where it reaches its maximum extension (B) before the pressure loss is decreased in this area while the cell of low pressure fluid leaves the evaluation plane (C). At the suction side boundary of the stator's wake the wake influence is shifted in time as the cell of high pressure fluid passes the evaluation plane later within the bar passing period. This process starts at $t/T = 2/8$ and is indicated by an area of lower total pressure loss coefficient (D) until it reaches its minimum values at $t/T = 3/8$ where larger areas of negative ζ_p are indicated via blanked values (E).

The vortex structures, the TEWV at first are strengthened and subsequently weakened, indicated by the shown contour isolines of Q-criterion (F). As described above, this phenomenon is caused by the positive and negative fluctuations of momentum transferred to the blade's boundary layer via the periodically incoming wakes. The evolution of the lower vortex system shows a continuous weakening of the HSV inside the evaluation plane (G). An analysis of the temporal evolution of the 3-dimensional vortex structures is presented in figure 11. For the sake of brevity only two time steps are shown. On the left side the HSV has its maximum extension ($t/T = 0$), whilst on the right side the HSV has its smallest extension ($t/T = 4/8$). The analysis revealed that further upstream (A) the pressure side HSV is deflected by the cells of high and low pressure inside the wake. This deflection causes the HSV to periodically impinge on the suction side near the area where the PV is affected by the corner separationn. (B). Due to this impingement the system consisting of PV and CSV is deflected towards midspan direction. Another effect is that the HSV loses momentum, which is observable inside the evaluation plane shortly thereafter. As a consequence of the weakened HSV a shift of PV and CSV back towards the endwalls is observable inside the evaluation plane at (H). This results in a fluctuating migration of the participating vortices in radial direction which is additionally influenced by the wake induced crossflow pressure gradient.

Phase 2 ($4/8 \leq t/T \leq 6/8$): Within this part the vortex structure located upstream of the incoming wake is passing the evaluation plane. At the suction side boundary of the stator's wake this passing is indicated by an emerging area of high total pressure loss (K) which is induced by the low pressure cell passing the evaluation plane. This area of high total pressure loss has its maximum extension around $t/T = 5/8$ (L) before it is weakened again (M) as the low pressure cell leaves the evaluation plane. At the pressure side boundary the high pressure cell causes a loss reduction with an area of negative ζ_p marked by blanked values (N). In the following time steps the total pressure loss in this area rises again (O).

The main vortex systems are further shifted towards the endwalls, weakened and reach their minimum extension around $5/8 \leq t/T \leq 6/8$ (P). This process is the continuation of the process described above in *Phase 1*. While both HSV are continuously weakened until $t/T = 5/8$ (Q), they get intensified at $t/T = 6/8$ until they reach their maximum extension around $0 \leq t/T \leq 7/8$ (R). The prominent fluctuation of the HSV can be explained by the above mentioned direct interaction of wake affected fluid and the HSV.

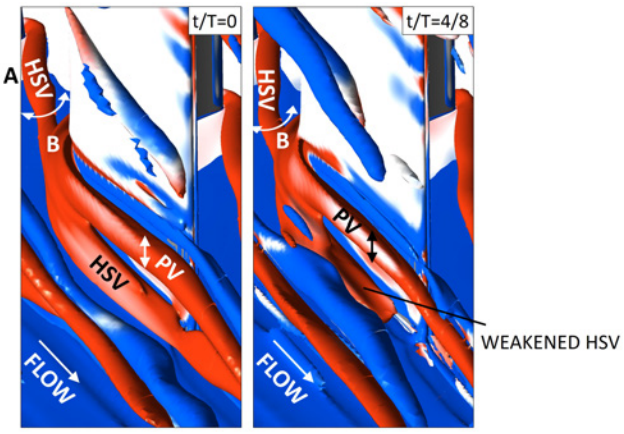

Figure 11. Distribution of secondary flow structures at two instants of time for $Sr = 1.35$, $\phi = 0.97$ visualized using Q-criterion iso surface at $Q(t) = 2 \cdot 10^5$ 1/s colored with vorticity ω_x

Phase 3 ($0 \leq t/T \leq 7/8$): During the third phase only fluid which is not affected by the wake passes the evaluation plane. In comparison to the time-averaged distribution in figure 7 the topology in this phase shows almost the same distribution of vortex structures and all vortex structures are clearly distinguishable. The HSVs are very pronounced, especially at the hub-side. The vortex systems consisting of PV & CSV are shifted towards midspan. This creates enough room for the HSV to spread and is a direct consequence of a strong corner separation which is caused by strong secondary flow. This TEWV system gets periodically suppressed by the incoming wakes which is in accordance to the findings of the experimental investigations by Sinkwitz *et al.* [8, 9] and can be explained by the transport of energy to the boundary layer described above.

6. SUMMARY AND CONCLUSION

In the present study URANS simulations of a large scale, low Mach number, annular turbine equipped with a newly designed T106^{RUB} LPT blading were conducted. The blading was modified to match the characteristics of the well known and frequently investigated T106 profile at low speed conditions. The results achieved by this simulations were compared with against stationary measurement data by means of static pressure distribution around the blade profile, integral flow values and 2-dimensional field traverse data and showed excellent agreement. The validation ensured that a detailed flow field analysis based on the CFD data is admissible. Well resolved CFD results were then used to identify the different vortex structures which interact in the secondary flow system of the investigated stator profile via an analysis of the 3-dimensional distribution of vortex structures visualized by the time averaged Q-criterion. The information

of this analysis were utilized to deduce the distribution of vortex structures inside the evaluation plane. Based on these findings a link between vortices and the distribution of axial vorticity was established supporting the interpretation of the experimental data.

An analysis of the wake kinematics revealed that the negative jet effect, caused by the periodically incoming wakes, induces two counter rotating vortices in front and behind the wake which extend in radial direction. As the wake affected fluid propagates through the passage these vortices create cells of low and high momentum fluid which affect boundary layers at blades and end walls.

A study of the temporal evolution of participating secondary flow structures revealed a strong interaction between the incoming wakes and the vortices, which are periodically weakened and intensified. It was found that the wake affected fluid causes a fluctuation of the pressure side legs of the horse shoe vortices, which interact with the passage vortices. This results in a radial shift of the passage vortices and concentrated shed vortices. In addition the horse shoe vortices get weakened due to the transfer of momentum into the passage vortices.

Regarding the distribution of total pressure loss on the evaluation plane, the temporal analysis revealed that the main impact on total pressure loss is caused by the cells of high and low pressure fluid inside the wake affected flow which causes a periodical reduction and rise of total pressure loss compared to the undisturbed flow.

It can be concluded that URANS simulations are capable of predicting the secondary flow structures for the underlying test case to a good degree of detail. Some minor deviations between CFD predictions and measurement are observed but the main vortex system is depicted very well.

ACKNOWLEDGMENTS

The investigations reported in this paper were conducted within the framework of the joint research project Unsteady Flow and Secondary Flow in Compressor and Turbine Cascades (PAK-530). The authors wish to gratefully acknowledge its funding and support by the Deutsche Forschungsgemeinschaft (DFG). The responsibility for the contents of this publication is entirely with the authors.

NOMENCLATURE

Latin Symbols

arc_{SS}	[m]	suction side arc length
c	[m/s]	absolute velocity
C	[m]	chord length
c_p	[-]	pressure coefficient
g	[-]	pitch
H	[m]	blade height
p	[Pa]	pressure
p_t	[Pa]	total pressure
Q	[$1/s^2$]	velocity invariant Q
r	[m]	radial coordinate
r'	[m]	transformed radial coordinate
Re	[-]	Reynolds number
S_{ij}	[1/s]	rate-of-strain tensor
Sr	[-]	Strouhal number
t	[s]	time
T	[s]	bar passing time
c_x	[m/s]	axial velocity
x	[m]	axial coordinate
x'	[m]	transformed axial coordinate

Greek Symbols

α	[°]	absolute velocity flow angle
ζ_p	[-]	pressure loss coefficient
θ	[°]	circumferential coordinate
ρ	[kg/m^3]	mass density
ϕ	[-]	flow coefficient
ω_x	[1/s]	axial vorticity
Ω_{ij}	[1/s]	vorticity tensor

Abbreviations

BC	boundary condition
CFD	computational fluid dynamics
CSV	concentrated shed vortex
CV	corner vortex
IGV	inlet guide vane
HSV	horseshoe vortex
PV	passage vortex
TEWV	trailing edge wake vortex
URANS	Unsteady Reynolds Averaged Navier-Stokes

REFERENCES

[1] V. Schulte and H. P. Hodson. Unsteady wake-induced boundary layer transition in high lift LP turbines. *ASME J. Turbomach.*, (128(1)):28–35, 1998.

[2] V. Michelassi, J. Wissink, and W. Rodi. Analysis of DNS and LES of flow in a low pressure turbine cascade with incoming wakes and comparison with experiments. *Flow Turbulence and Combustion*, 69(3-4):295–329, 2002.

[3] V. Michelassi, J. Wissink, J. Fröhlich, and W. Rodi. Large-eddy simulation of flow around low-pressure turbine blade with incoming wakes. *AIAA Journal*, 41(11):2143–2156, 2003.

[4] V. Michelassi, L.-W. Chen, R. Pichler, and R. D. Sandberg. Compressible direct numerical simulation of low-pressure turbines: Part II — effect of inflow disturbances. *ASME J. Turbomach.*, 137(7), 2015.

[5] V. Michelassi, L.-W. Chen, R. Pichler, R. D. Sandberg, and R. Bhaskaran. High-fidelity simulations of low-pressure turbines: Effect of flow coefficient and reduced frequency on losses. *ASME J. Turbomach.*, Nov 2016.

[6] D. Koschichow, J. Fröhlich, R. Ciorciari, I. Kirik, and R. Niehuis. Numerical and experimental investigation of

the turbulent flow through a low-pressure turbine cascade in the endwall region. Number 13, pages 311–312. Proceedings in Applied Mathematics and Mechanics.

[7] D. Koschichow, J. Fröhlich, I. Kirik, and R. Niehuis. DNS of the flow near the endwall in a linear low pressure turbine cascade with periodically passing wakes. Number GT2014-25071. Proceedings of ASME Turbo Expo 2014.

[8] M. Sinkwitz, B. Winhart, D. Engelmann, F. di Mare, and R. Mailach. Experimental and numerical investigation of secondary flow structures in an annular LPT cascade under periodical wake impact – part 1: Experimental results. Proceedings of ISROMAC, Maui, Hawaii, December 16-21 2017.

[9] M. Sinkwitz, D. Engelmann, and R. Mailach. Experimental investigation of periodically unsteady wake impact on secondary flow in a 1.5 stage full annular LPT cascade with modified T106 blading. Number GT2017-64390. Proceedings of ASME Turbo Expo, Charlotte, NC, USA, June 26-30 2017.

[10] G. Schneider and M. Raw. Control volume finite-element method for heat transfer and fluid flow using collocated variables – 1. computational procedure. *Numerical Heat Transfer*, 11(4):363–390, 1987.

[11] B. Winhart, D. Micallef, and D. Engelmann. Application of the time transformation method for a detailed analysis of multistage blade row interactions in a shrouded turbine. Number ETC2017-094. Proceedings of 12th ETC, April 3-7, 2017; Stockholm, Sweden.

[12] F. Menter. Two-equation eddyviscosity turbulence models for engineering applications. *AIAA Journal*, 23(8):1598–1605, 1994.

[13] F. Menter, P.E. Smirnov, T. Liu, and R. Avancha. A one-equation local correlation-based transition model. *Flow, Turbulence and Combustion*, July 2015.

[14] V. Kolář. Vortex identification: New requirements and limitations. *International Journal of Heat and Fluid flow*, pages 638–652, 2007.